Acta Crystallographica Section D
Biological Crystallography
ISSN 0907-4449

Structure of insect-cell-derived IL-22

Ting Xu,[a,b] Naomi J. Logsdon[a] and Mark R. Walter[a,b]*

[a]Center for Biophysical Sciences and Engineering, University of Alabama at Birmingham, Birmingham, AL 35294, USA, and [b]Department of Microbiology, University of Alabama at Birmingham, Birmingham, AL 35294, USA

Correspondence e-mail: walter@uab.edu

Received 17 January 2005
Accepted 28 March 2005

PDB Reference: insect-cell-expressed IL-22, 1ykb, r1ykbsf.

The crystal structure of interleukin-22 expressed in *Drosophila melanogaster* S2 cells (IL-22_{Dm}) has been determined at 2.6 Å resolution. IL-22_{Dm} crystals contain six molecules in the asymmetric unit. Comparison of IL-22_{Dm} and IL-22_{Ec} (interleukin-22 produced in *Escherichia coli*) structures reveals that N-linked glycosylation causes only minor structural changes to the cytokine. However, 1–4 Å main-chain differences are observed between the six IL-22_{Dm} monomers at regions corresponding to the IL-22R1 and IL-10R2 binding sites. The structure of the carbohydrate and the conformational variation of $IL22_{Dm}$ provide new insights into IL-22 receptor recognition.

1. Introduction

Interleukin-22 (IL-22) is a α-helical cytokine produced by activated T cells (Dumoutier, Louahed *et al.*, 2000; Xie *et al.*, 2000). IL-22 upregulates the production of early systemically circulated defense proteins (acute phase proteins) such as serum amyloid A, α1-chemotrypsin and haptoglobin in liver cells (Dumoutier, Van Roost *et al.*, 2000). IL-22 also induces pancreatitis-associated protein, PAP1, in acinar cells (Aggarwal *et al.*, 2001) and the antimicrobial proteins β-defensin 2 and 3 and psoriasin in human karatinocytes (Wolk *et al.*, 2004). The data suggest that the normal cellular function of IL-22 is to provide innate non-specific immunity against invading pathogens in skin and other tissues. However, high levels of IL-22 are observed in T-cell-activated skin diseases and preliminary data suggest that IL-22 may be an important mediator of chronic systemic inflammation (Wolk *et al.*, 2004).

IL-22 is member of the class-2 cytokine family, which includes IL-10, IL-19, IL-20, IL-24 and IL-26 (Walter, 2002, 2004; Fickenscher *et al.*, 2002; Pestka *et al.*, 2004). Class-2 cytokines share ~25% sequence identity and largely conserve an IL-10 footprint sequence (Walter & Nagabhushan, 1995; Walter, 2004). The crystal structure of IL-22 produced in *Escherichia coli* (IL-22_{Ec}) has been determined (Nagem *et al.*, 2002). IL-22_{Ec} exists as a α-helical monomer that is structurally similar to each subunit of the IL-10 dimer (Logsdon *et al.*, 2002; Nagem *et al.*, 2002). However, in contrast to IL-10, IL-22 expressed in eukaryotic cells is glycosylated at three different N-linked glycosylation sites (Asn-*X*-Ser/Thr, where *X* is any amino acid) corresponding to Asn54, Asn68 and Asn97 (Kotenko *et al.*, 2001; Dumoutier, Louahed *et al.*, 2000).

IL-22 cellular activities are mediated through a heterodimeric receptor complex consisting of the cell-surface receptor chains IL-22R1 and IL-10R2 (Kotenko *et al.*, 2001; Xie *et al.*, 2000; Dumoutier, Louahed *et al.*, 2000; Dumoutier, Van Roost *et al.*, 2000). IL-22R1 and IL-10R2 are members of

Table 1
Data-collection and refinement statistics.

Values in parentheses are for the highest resolution shell.

Data-collection statistics	
Space group	$P2_1$
No. of molecules in AU	6
Rocking curve (°)	0.8
Crystallization temperature(K)	310
Data-collection temperature (K)	100
Unit-cell parameters	
a (Å)	64.88
b (Å)	62.23
c (Å)	139.52
β (°)	91.35
Wavelength (Å)	1.255
Resolution (Å)	50–2.6 (2.69–2.60)
No. of observations	108300
No. of unique observations	32705 (2720)
Redundancy	3.3 (2.8)
Completeness (%)	94.5 (79.5)
$I/\sigma(I)$	21.3 (2.1)
$R_{\rm merge}$(%)	0.051 (0.344)
Wilson B factor (Å^2)	63.8
Refinement statistics	
R factor	0.232 (0.354)
No. of reflections (working set)	31111
$R_{\rm free}$	0.265 (0.371)
No. of reflections (test set)	1651
No. of protein atoms	6876
No. of carbohydrate atoms	252
No. of water atoms	51
No. of atoms in alternate conformations	18
Geometry	
R.m.s.d. bond distance (Å)	0.01
R.m.s.d. bond angles (°)	1.34
R.m.s.d. B (Å^2)	
Main-chain atoms	1.62
Side-chain atoms	2.24
Average B (Å^2)	
Overall	60.30
Protein atoms	59.8
Carbohydrate atoms	81.2
Water atoms	44.6
Ramachandran plot	
Most favored region (%)	92.5
Additionally allowed regions (%)	7.5
Generously allowed regions (%)	0.0
Disallowed regions (%)	0.0

the class-2 cytokine family first described by Bazan (1990*a*,*b*). The extracellular domains of IL-22R1 and IL-10R2 share ∼13% sequence identity and are structurally related to the high-affinity IL-10 receptor (IL-10R1), the crystal structure of which has been determined (Josephson *et al.*, 2001). Formation of the IL-22/IL-22R1/IL-10R2 ternary complex activates the JAK/STAT and MAP kinase signaling pathways, which leads to the induction of IL-22-specific genes (Fig. 1; Lejeune *et al.*, 2002). Surface plasmon resonance (SPR) studies performed with the soluble extracellular receptor fragments reveal that the IL-22R1 chain exhibits approximately a 600-fold higher affinity for IL-22 ($K_{\rm d} \simeq 20$ nM) than IL-10R2 ($K_{\rm d} \simeq 120$ μM) (Logsdon *et al.*, 2004). The affinity of soluble IL-10R2 for the IL-22/IL-22R1 binary complex ($K_{\rm d} \simeq 14$ μM) is about tenfold higher than for IL-22 alone ($K_{\rm d} \simeq 120$ μM). Furthermore, N-linked glycosylation attached to Asn54 enhances IL-10R2 binding to IL-22 alone or the IL-22/sIL-22R1 complex by approximately eightfold and is required for maximal biological responses as measured by luciferase reporter assays (Logsdon *et al.*, 2004).

Here, we report the crystal structure of IL-22 expressed in *Drosophila melanogaster* S2 cells (IL-22$_{\rm Dm}$) that contains N-linked carbohydrate at each N*X*S/T glycosylation site. IL-22$_{\rm Dm}$ crystallizes with six IL-22$_{\rm Dm}$ monomers in the asymmetric unit. Comparison of IL-22$_{\rm Dm}$ and IL-22$_{\rm Ec}$ structures reveals that N-linked glycosylation causes only minor structural changes to the cytokine. However, 1–4 Å main-chain differences are observed between the six IL-22$_{\rm Dm}$ monomers at regions corresponding to the IL-22R1 and IL-10R2 binding sites, as defined by an IL-22/IL-22R1 homology model (Logsdon *et al.*, 2002) and alanine-scanning mutagenesis (Logsdon *et al.*, 2004), respectively. The structure of the carbohydrate and the conformational variation of IL22$_{\rm Dm}$ provide new insights into IL-22 receptor recognition.

2. Materials and methods

2.1. Protein expression, purification and crystallization

IL-22 was expressed and crystallized as previously described (Xu *et al.*, 2004). Briefly, IL-22 was secreted from Sshcneider 2 *D. melanogaster* cells (IL-22$_{\rm Dm}$) and purified from the culture media using nickel-affinity chromatography. The histidine tag was cut with factor Xa protease and removed from the sample by anion-exchange chromatography. Mass spectrometry revealed that purified IL-22$_{\rm Dm}$ consists of six different glycosylation variants, including molecules with zero, one, two or three N-linked glycans (Xu *et al.*, 2004). Crystals of IL-22$_{\rm Dm}$ were only obtained after an additional cation-exchange purification step that significantly enriched for IL-22$_{\rm Dm}$ molecules with glycans attached to all three N-linked glycosylation sites: Asn54, Asn68 and Asn97. IL-22$_{\rm Dm}$ crystals were grown at 310 K from drops containing 100 mM trisodium citrate buffer pH 6.0, 0.2 M ammonium acetate, 1.4 mM cetyltrimethylammonium bromide (CTAB) incubated over a reservoir of 20% PEG 4000.

2.2. Data collection

For data collection, an IL-22$_{\rm Dm}$ crystal was soaked for 1 min in a cryosolution containing 0.1 M trisodium citrate pH 6.0, 0.2 M ammonium acetate and 29% PEG 4000 at 310 K. The crystal was flash-cooled by transferring it from the cryosolution to a nitrogen-gas stream at 100 K. Diffraction data were collected at the Advance Photon Source (SERCAT ID22 beamline). A total of 180 1° oscillation images (1 s exposure time) were collected at a wavelength of 1.255 Å. The data were indexed, integrated and scaled using *HKL*2000 (Otwinowski & Minor, 1997). Intensities were converted to structure-factor amplitudes using the program *TRUNCATE* within the *CCP*4 package (Collaborative Computational Project 4, Number 4, 1994; Winn *et al.*, 2002). Statistics of data collection are shown in Table 1.

2.3. Structure determination

The structure was solved by molecular replacement using the program *BEAST* (Read, 2001) with data between 15 and 4 Å resolution and the coordinates of IL-22$_{Ec}$ (PDB code 1m4r, chain *A*; Nagem *et al.*, 2002) as the search model. The model was rigid-body refined, followed by several cycles of simulated-annealing and conjugate-gradient minimization refinements performed in *CNS* v.1.1 using the maximum-likelihood target function (Brünger *et al.*, 1998; Adams *et al.*, 1997). Prior to refinement, 5% of the data were randomly omitted for monitoring of the free *R* factor (Brünger, 1992). Manual rebuilding of the model was performed using the graphics program *O* with $2F_o - F_c$ and $F_o - F_c$ maps calculated using *SIGMAA*-weighted coefficients to help reduce model bias. Non-crystallographic symmetry (NCS) restraints were used throughout the refinement (Table 2) as well as corrections for bulk solvent and anisotropy in the diffraction data (Jiang & Brünger, 1994). Protein, carbohydrate and water molecules were added until no further interpretation of $F_o - F_c$ maps was possible. Refinement progress was monitored by R_{free}, improvement in the geometry of the model was monitored using *PROCHECK* (Laskowski *et al.*, 1993) and improvement in the fit of the model to the map was monitored based on visual inspection and real-space *R* correlation coefficients calculated with *MAPMAN* (Kleywegt & Jones, 1996). The final refinement statistics are presented in Table 1. Superpositions were performed using the algorithm of Kabsch (1976). Buried surface area was calculated with *AREAIMOL* from the *CCP*4 program suite using a probe radius of 1.4 Å (Winn *et al.*, 2002). Secondary structure was defined using the algorithm of Kabsch & Sander (1983) as implemented in *RIBBONS* (Carson, 1997), which was also used to generate Figs. 2–5, 7 and 8.

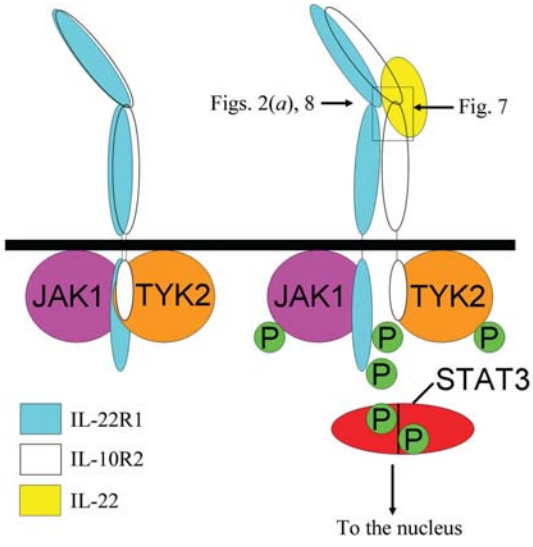

Figure 1
Schematic model of the IL-22/IL-22R1/IL-10R1 signaling complex. IL-22-mediated assembly of the ternary receptor complex activates both JAK/STAT and MAP kinase signaling pathways (Lejeune *et al.*, 2002). Only the JAK kinases and STAT3 are shown in the figure, although IL-22 also activates STAT1 and STAT5 at reduced levels (Lejeune *et al.*, 2002). Fluorescence resonance energy transfer (FRET) data collected on the IFN-γ receptor complex suggests that class-2 cytokines induce signaling by separating the intracellular domains of the receptors (Krause *et al.*, 2002). IL-22 receptor-complex assembly activates the JAK kinases, resulting in phosphorylation of IL-22R1, JAK1, TYK2 and STAT3. Phosphorylated STAT3 dimers translocate to the nucleus where they activate gene transcription, resulting in IL-22 cellular responses. The orientation of Figs. 2(*a*) and 8 are shown on the complex by an arrow. The view in Fig. 7 corresponds to the box shown in the figure. The color codes for the receptors and IL-22 are shown in the figure.

Table 2
Non-crystallographic symmetry restraints.

Group 1	
Chains	*A*, *D*, *F*
Residues	42–67, 74–103, 111–129, 134–179
Side chains omitted	44, 54, 58, 67, 77, 81, 88, 112, 116, 124, 125, 127, 128, 137–140, 143, 144, 153, 154, 157, 172, 175
NCS weight, sigb	100.0, 2.0
R.m.s.d (Å)	
A–*D*	0.085
A–*F*	0.077
Group 2	
Chains	*B*, *C*, *E*
Residues	42–47, 53–67, 74–103, 111–129, 134–179
Side chains omitted	44, 58, 67, 77, 81, 88, 112, 116, 124, 125, 127, 128, 137–140, 143, 144, 153, 154, 157, 172, 175
NCS weight, sigb	100.0, 2.0
R.m.s.d (Å)	
B–*C*	0.083
B–*E*	0.086

Table 3
Residues and carbohydrate in the IL-22$_{Dm}$ structure.

		Glycosylation		
Chain	Residues	Asn54	Asn68	Asn97
A	39–179	$(GlcNAc)_2$-Fuc	—	GlcNAc
B	38–179	—	—	GlcNAc
C	38–179	—	—	$(GlcNAc)_2$
D	38–179	$(GlcNAc)_2(Man)_2$-Fuc	—	$(GlcNAc)_2$
E	38–179	—	—	GlcNAc
F	38–179	$(GlcNAc)_2$	—	$(GlcNAc)_2$

3. Results and discussion

3.1. Quality of the model

The structure of IL-22$_{Dm}$ was solved by molecular replacement and refined at 2.6 Å resolution to an *R* factor of 23.3% and an R_{free} of 26.5% (Table 1). The crystallographic asymmetric unit contains six IL-22$_{Dm}$ monomers (monomers *A*–*F*) that are related by non-crystallographic symmetry (Table 2), resulting in a solvent content of 44.6% (Fig. 2). Interpretable electron density was observed for residues 39–179 of monomer *A* and 38–179 of monomers *B*–*F*, as well as nine carbohydrate chains and 51 water molecules (Table 3). Of the 851 amino acids in the asymmetric unit, 92.5% are in the most favored region of the Ramachandran plot and the remaining 7.5% are in the additionally allowed region as defined in *PROCHECK* (Laskowski *et al.*, 1993). As previously described for IL-22$_{Ec}$, Pro113, located just before the start of helix *D*, adopts a *cis* conformation in each monomer. Alternate conformations were built for residues

Met*A*58, Arg*A*128, Met*B*58, Leu*C*125, Met*D*58, Arg*D*175 and Arg*F*175, where each residue is described by amino-acid type, chain identifier and residue number.

3.2. The IL-22$_{Dm}$ monomer

The IL-22$_{Dm}$ monomers consist of six α-helices (*A*–*F*) that form a compact bundle as previously described for IL-22$_{Ec}$ (Nagem *et al.*, 2002; Fig. 2*a*). The helices are 4–23 residues in length and, with the exception of helix *F*, are essentially straight (Table 4). Preceding helix *A*, residues 44–47 form a single turn of 3_{10}-helix (pre-*A*) that is oriented at approximately 90° to helix *A* (residues 50–65). The pre-*A* helix is stabilized by four distinct hydrogen bonds (Asp43 O$^{\delta1}$–Ser45 N, Asp43 O$^{\delta1}$–Ser45 O$^{\gamma1}$, Asp43 O–Asn46 N$^{\delta1}$, Ser45 O–Gln49 N$^{\varepsilon1}$) formed by Asp43, Ser45, Asn46 and Gln49 (Fig. 3).

There is some variation in the assignment of secondary structure to helices *A*, *B*, *C* and *D* (Table 4). Helix *A* begins at Thr52, rather than Pro50, in monomers *B* and *E* because of a large structural change of residues Gln49 and Pro50 that is discussed in more detail below. Helix *B* (residues 77–80) is observed in either a 3_{10}- or α-helical conformation in both IL-22$_{Dm}$ and IL-22$_{Ec}$ monomers. Similar secondary-structure variations are observed for residues 85–87, although visual inspection suggests this segment is most like a 3_{10}-helix in all eight IL-22 monomer structures analyzed. The last α-helical residue in helix *C* is Glu102. However, the helix extends to Phe105 by the formation of a π-helix that is characterized by *i* to *i* + 5 hydrogen bonding between Thr99/Leu104 and Leu100/Phe105. A similar π-helix has previously been described in helix *C* of IL-10 and IL-19 (Walter & Nagabhushan, 1995; Chang *et al.*, 2003). The C-terminal end of helix *E* (residues 129–131) adopts a 3_{10}-helix in IL-22$_{Dm}$ monomers but not in IL-22$_{Ec}$. This secondary-structure difference is accompanied by 1.5–3 Å differences in the position of Thr131 between the IL-22$_{Dm}$ and IL-22$_{Ec}$ monomers. Since this region of IL-22$_{Ec}$ is involved in a crystal contact, it is likely that the 3_{10}-helix is the predominant conformation in solution. Finally, helix *F* exhibits an ∼51° bend characteristic of the class-2 α-helical cytokines (IFN-γ, IL-10 and IL-19) that divides the helix into two parts: F_1 and F_2 (Walter, 2004).

IL-22$_{Dm}$ contains two disulfide bonds (Fig. 2*a*). The first connects Cys40 at the N-terminus with Cys130 located at the C-terminus of helix *D*. The second joins Cys89, located on helix *C*, with Cys178 on helix *F*. The helices are joined by peptide segments (loops) that exhibit irregular secondary structure. Residues 68–73 in the *AB* loop and 134–135 in the *DE* loop exhibit weak side-chain density and high *B* factors in the structure.

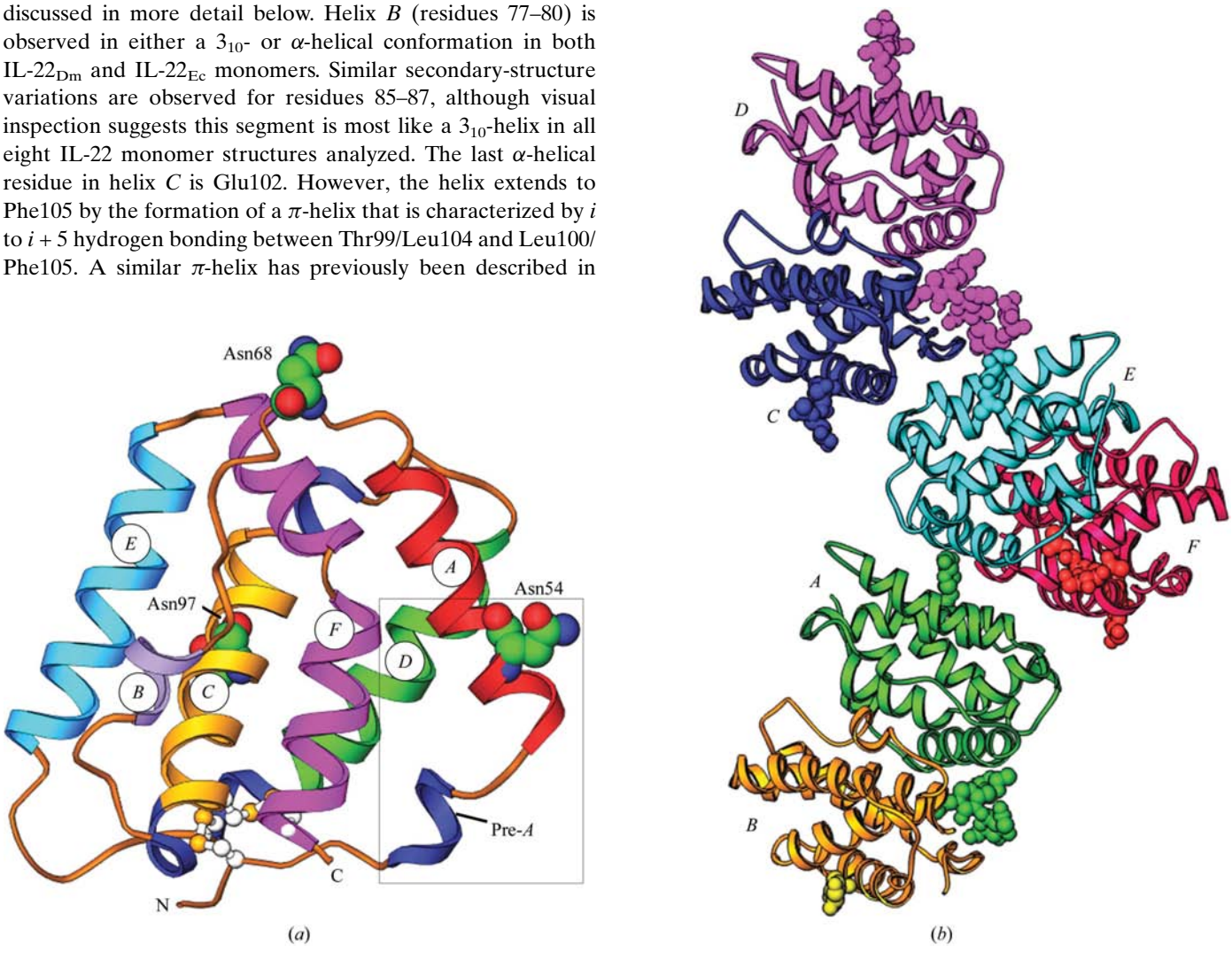

Figure 2
Structure of IL-22$_{Dm}$. (*a*) Ribbon diagram of the IL-22$_{Dm}$ monomer. Asparagines that are modified by N-linked glycosylation are shown. The boxed region corresponds to the region shown in Fig. 3. (*b*) Packing in the asymmetric unit of the IL-22$_{Dm}$ cell. Ribbon diagram of the six NCS-related IL-22$_{Dm}$ monomers labeled by chain identifier (*A*–*F*). N-linked glycosylation attached to each monomer is shown in space-filling format and colored the same as the ribbon to which it is attached.

Table 4
IL-22 secondary-structure comparison.

Ec*A* and Ec*B* correspond to the *A* and *B* chains of IL-22$_{Ec}$, respectively.

	A	*B*	*C*	*D*	*E*	*F*	Ec*A*	Ec*B*
Pre-*A*, 3_{10}	44–47	44–47	44–47	44–47	44–47	44–47	44–47	44–47
Helix *A*, α	50–64	52–65	51–65	50–64	52–65	50–64	50–64	50–64
Helix *B*, α	77–80	—	—	77–80	—	77–80	77–80	—
Helix *B*, 3_{10}	—	77–80	77–80	—	77–80	—	—	77–80
Helix *C*, 3_{10}	85–87	—	—	85–87	—	85–87	—	85–87
Helix *C*, α	88–102	88–102	85–102	88–102	85–102	88–101	88–102	88–102
Helix *D*, α	115–128	114–129	114–129	115–128	114–128	115–128	115–129	114–128
Helix *D*, 3_{10}	129–131	—	—	129–131	129–131	129–131	—	—
Helix *E*, α	139–154	139–154	139–154	139–154	139–154	139–154	139–155	139–154
Helix F_1, α	156–165	156–164	156–164	156–165	156–164	156–165	157–165	157–165
Helix F_2, α	167–178	167–178	167–178	167–178	167–178	167–178	167–178	167–178

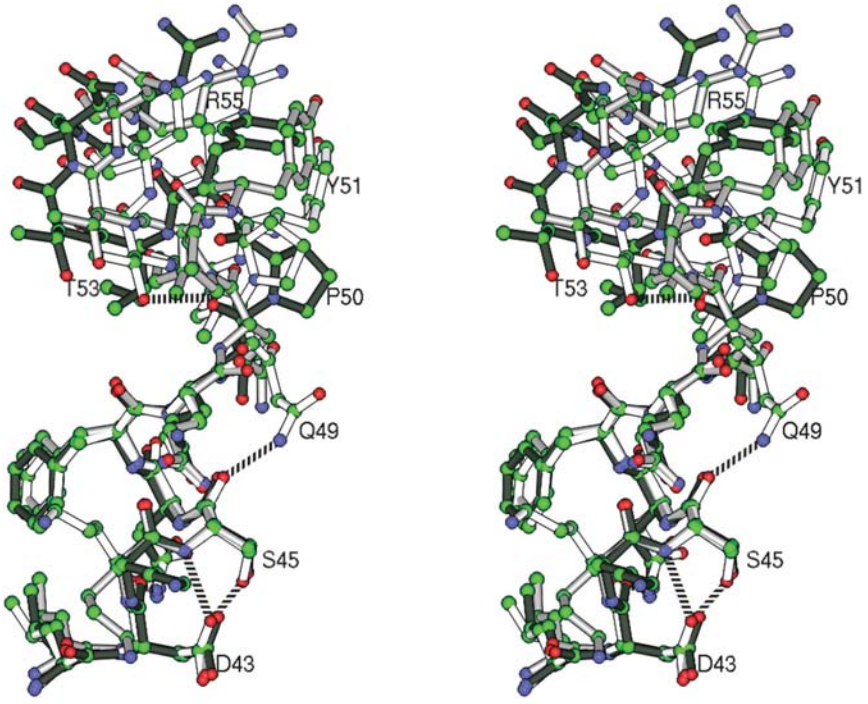

Figure 3
Sterero diagram of pre-*A*/helix *A* region. Ball-and-stick models of IL-22$_{Dm}$ residues 42–55 corresponding to conformation 1 in monomers *A*, *D* and *F* (white), conformation 2 in monomers *B* and *E* (black) and conformation 3 in monomer *C* (silver) are shown. C, O and N atoms are colored green, red and blue, respectively. For the figure, the pre-*A* regions (residues 43–47) were superimposed to show the conformational differences clearly.

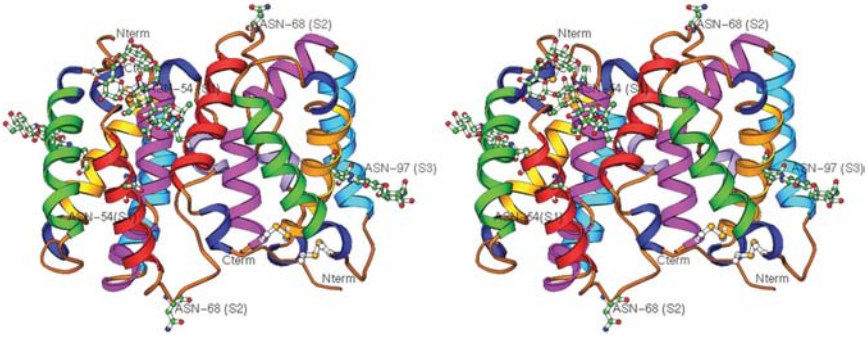

Figure 4
Sterero diagram of the IL-22$_{Dm}$ dimer. The NCS-related monomers *C* (left) and *D* (right) along with their attached carbohydrates. The color coding of the IL-22$_{Dm}$ monomers is as in Fig. 2(*a*).

3.3. Organization of IL-22$_{Dm}$ monomers in the asymmetric unit

The six IL-22$_{Dm}$ monomers (*A*–*F*) form three non-covalent dimers (monomers *AB*, *CD* and *EF*) that are related to one another by an approximate non-crystallographic twofold screw axis (translation ∼36 Å) parallel to the *c* axis (Fig. 2). The monomers in each dimer are also related to one another by NCS twofold screw axes (translation of ∼6.7 Å) perpendicular to the axes of their helix bundles (Fig. 4). This dimeric arrangement was previously observed in the structure of IL-22$_{Ec}$, which contains one dimer (monomers Ec*A* and Ec*B*) in the crystallographic asymmetric unit. In IL-22$_{Dm}$, the dimer interface is formed by residues Lys44–Arg88, which extend from the pre-*A* helix to the beginning of helix *C*, and Gly168–Ile179, corresponding to helix F_2 in both monomers. A total of 2460 Å^2 of solvent-accessible surface area is buried in the IL-22$_{Dm}$ dimer interface, compared with 2345 Å^2 for the IL-22$_{Ec}$ dimer. The additional surface area buried in the IL-22$_{Dm}$ dimer interface is owing to carbohydrate attached to Asn54 in monomers *A*, *D* and *F*.

3.4. Glycosylation

The IL-22 amino-acid sequence contains three N-linked glycosylation sites (Asn-*X*-Ser/Thr) corresponding to Asn54 located at the N-terminal end of helix *A*, Asn68 in the *AB* loop and Asn97 located in the center of helix *C* (Fig. 2*a*). Characterization of IL-22$_{Dm}$ by mass spectrometry reveals hexasaccharides consisting of two *N*-acetyl glucosamines (GlcNAc), three mannose (Man) residues and a fucose moiety (Fuc) to be attached to Asn54, Asn68 and Asn97

(Xu *et al.*, 2004). The six monomers in the asymmetric unit contain a total of 18 possible N-linked glycosylation sites (3 × 6 monomers). However, only nine carbohydrate chains, of different lengths, are observed in the electron density (Table 3). Observed glycans are attached to Asn54 of monomers *A*, *D* and *F* and the remaining six are attached to Asn97 (Fig. 2*a*). No electron density is observed for carbohydrate attached to Asn68 in any of the six NCS-related IL-22_{Dm} monomers.

The presence or absence of visible electron density for the carbohydrate residues is correlated with intramolecular or intermolecular contacts with IL-22_{Dm}. The side chains of Asn54 and Asn68 extend away from the surface of the protein, while Asn97 is located in a small cavity between the side chains of Glu101 and Ser126 (Fig. 5). Because the carbohydrate chains attached to Asn54 and Asn68 do not form intramolecular contacts with IL-22_{Dm} they are very mobile, explaining the lack of density at three of the six Asn54 residues and all six Asn68 residues. Electron density is observed for carbohydrate residues attached to Asn54 of monomers *A*, *D* and *F* because they form intermolecular contacts with the NCS-related monomers *B*, *C* and *E* in the dimer interface (Fig. 4). Approximately 130 Å^2 of the 190 Å^2 of carbohydrate surface area buried in the dimer interface is contributed by the first GlcNAc attached to the N$^{\delta1}$ atom of Asn54. Each GlcNAc also forms an intermolecular hydrogen bond between the O$^{\gamma}$ atom of Thr53 and O7 of the GlcNAc. Despite these contacts, the protein atoms surrounding the GlcNAcs are in the same conformation as observed in the IL-22_{Ec} structure.

In contrast to the highly mobile carbohydrate chains attached to Asn54 and Asn68, electron density is observed for at least one GlcNAc attached to Asn97 in all six IL-22_{Dm} monomers. This is most likely to be because the GlcNAc attached to Asn97 forms two intramolecular hydrogen bonds with IL-22_{Dm} (Fig. 5). The first is between Glu101 O$^{\gamma1}$ and the N atom of the GlcNAc. The second occurs between Ser126 O$^{\gamma}$ and the O atom of the GlcNAc acetyl moiety. In the absence of glycosylation, as represented by the structure of IL-22_{Ec}, Asn97 O$^{\delta1}$ hydrogen bonds to Ser126 O$^{\gamma}$. Apart from this side-chain rearrangement, the region surrounding Asn97 is essentially identical in the IL-22_{Dm} and IL-22_{Ec} structures.

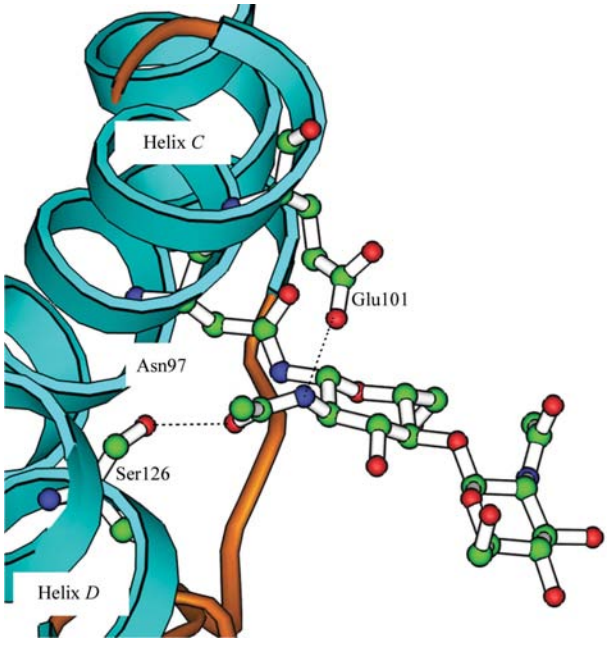

Figure 5
The GlcNAc environment around Asn97. The disaccharide, Ser126 and Glu101 are shown as ball-and-stick models. Hydrogen bonds are shown as dashed lines.

3.5. Conformational differences between NCS-related IL-22_{Dm} monomers

The overall root-mean-square deviation (r.m.s.d.) between the six NCS-related IL-22_{Dm} monomers (C$^{\alpha}$ atoms 39–179) ranges from 0.23 to 0.97 Å (Table 5). Monomers *A*, *D* and *F* (r.m.s.d.s 0.23–0.32 Å) are most similar to one another and to monomer Ec*A* (*A* chain) from IL-22_{Ec} (r.m.s.d $\simeq$ 0.56–0.59 Å). Similarly, monomers *B*, *C* and *E* exhibit lower r.m.s.d. values with one another (r.m.s.d.s 0.32–0.53 Å) than with monomers *A*, *C* and *E*. The largest main-chain deviations occur for residues 43–57, which include the pre-*A* helix and the N-terminal end of helix *A*, as well as residues 68–73 located in the *AB* loop (Fig. 6).

In all six IL-22_{Dm} monomers, *AB*-loop residues 68–73 exhibit equally large (1–2 Å) main-chain differences. In contrast, residues 43–57 adopt three distinct conformations (conformations 1, 2 and 3) caused by rigid-body movements of the pre-*A* helix and helix *A* segments by 1–4 Å from one another. These structural differences are correlated with unique NCS and crystal-packing contacts encountered by

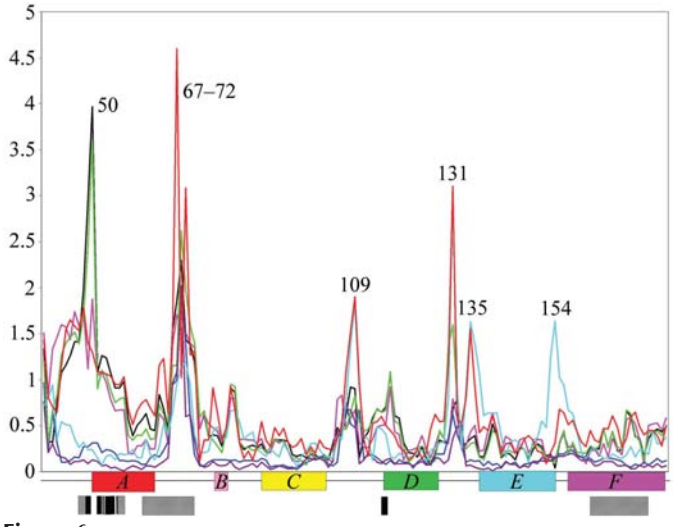

Figure 6
Main-chain differences between IL-22 monomers. Main-chain differences (Å, *y* axis), relative to monomer *A*, are plotted against residue number (*x* axis). Differences are plotted for monomers *B* (black), *C* (magenta), *D* (blue), *E* (green), *F* (purple) and IL-22_{Ec} monomer *A* (cyan) and IL-22_{Ec} monomer *B* (red). The secondary structure of IL-22 is shown below the *x* axis, with helices shown as rectangles and colored as shown in Fig. 2(*a*). The location of the IL-22R1 (striped rectangles) and IL-10R2 (black rectangles) binding sites are shown below the secondary-structure chart. Residue labels are shown for regions that exhibit main-chain differences of >1 Å.

different IL-22_{Dm} monomers. Contacts in the dimer interface are asymmetric, with Asp43–Phe57 from monomers *A*, *D* and *F* burying 380 Å^2 of surface area into the interface and monomers *B*, *C* and *E* burying 240 Å^2. Of the 240 Å^2 of surface area buried in monomers *B*, *C* and *E*, 130 Å^2 is owing to the first GlcNAc attached to Asn54 (in monomers *A*, *D* and *F*) rather than protein–protein contacts. Additional and essentially identical crystal contacts are observed in the pre-*A* helix region of monomers *A*, *D* and *F*, while no contacts are formed with the pre-*A* helix of monomers *B* and *E*. The pre-*A* region in monomer *C* is involved in a crystal contact that differs from monomers *A*, *D* and *F*. As a result, Asp43–Phe57 in monomers *A*, *D* and *F* adopt one conformation (conformation 1), monomers *B* and *E* adopt a second conformation (conformation 2) and monomer *C* adopts a third conformation (conformation 3) (Fig. 3).

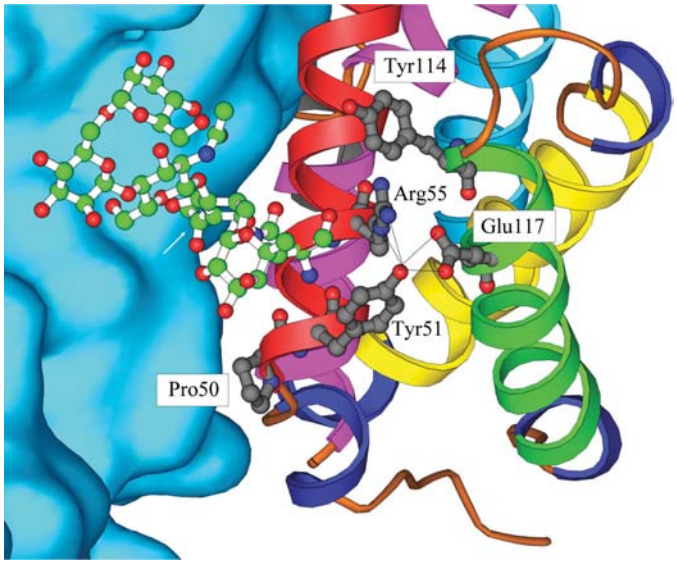

Figure 7
The IL-10R2 binding site in the context of the IL-22/IL-22 homology model. The ribbon diagram of IL-22_{Dm} monomer *D* is colored as described in Fig. 2(*a*). The accessible surface of the IL-22R1 chain is shown in cyan. The position of the glycan attached to Asn54 with the modeled side-chain rotamer ($\chi_1 = -174°$, $\chi_2 = 20°$) is shown. Hydrogen binding for side chains involved in IL-10R2 interactions are denoted by dashed lines. An arrow (white) denotes the location of the *N*-acetyl group of the first GlcNAc.

Table 5
Superposition of IL-22 molecules r.m.s.d. values (Å) for C$^\alpha$ atoms 39–179.

	A	*B*	*C*	*D*	*E*	*F*	Ec*A*	Ec*B*
A	—							
B	0.77	—						
C	0.67	0.53	—					
D	0.32	0.74	0.69	—				
E	0.76	0.32	0.53	0.73	—			
F	0.28	0.71	0.64	0.23	0.71	—		
Ec*A*	0.59	0.90	0.87	0.56	0.94	0.59	—	
Ec*B*	0.90	0.95	0.90	0.95	0.97	0.95	0.91	—

In the absence of crystal contacts, Gln49 and Pro50 in monomers *B* and *E* adopt main-chain conformations that differ by about 2.9 and 4 Å from their positions in monomers *A*, *D* and *F* (Figs. 3 and 6). Gln49 and Pro50 appear to provide a flexible pivot point that allows the pre-*A* region and N-terminus of helix *A* to undergo the rigid-body movements that define conformations 1–3 (Fig. 3). Structural differences in the pre-*A* region and helix *A* regions reorients the side chain of Tyr51 and results in 0.6–1 Å main-chain differences for Tyr114–Glu117 located on helix *D*. In monomers *A*, *D* and *F*, helices *A* and *D* are coupled by side-chain hydrogen-bond/salt-bridge interactions between Tyr51, Arg55 and Glu117 as shown in Fig. 7. However, these interactions are disrupted in monomers *B*, *C* and *E*.

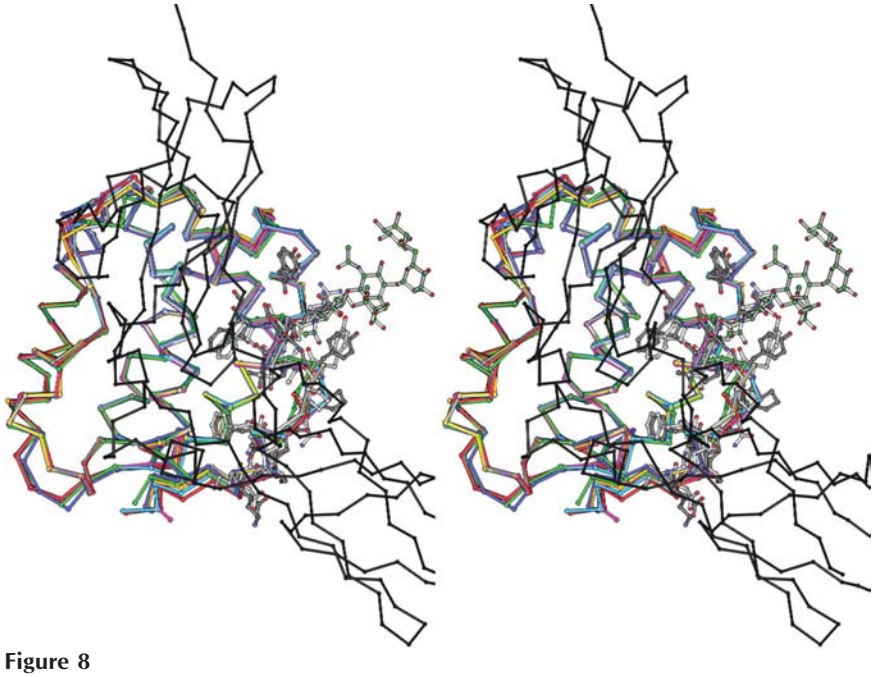

Figure 8
Stereo diagram of the IL-22/IL-22R1 homology model. C$^\alpha$ traces for IL-22_{Dm} monomers (*A*–*D* and IL-22_{Ec} chains Ec*A* and Ec*B*) are shown and colored as described in Fig. 2(*a*). Ball-and-stick representations are shown for residues 42–57, 114 and 117 for IL-22Dm monomers *B* (grey) and *E* (white). Atoms are colored as described in Fig. 3. The C$^\alpha$ atoms of the IL-22R1 chain are shown in black.

3.6. Implications for receptor binding

A homology model of the IL-22/sIL-22R1 complex was previously built using the IL-10/sIL-10R1 structure (Josephson *et al.*, 2001; Logsdon *et al.*, 2002). This model predicts that IL-22R1 contacts IL-22 residues located on pre-*A* (residues 47–48), helix *A*, the *AB* loop (residues 53, 57, 61–73) and helix *F* (residues 162–175) (Figs. 6 and 8). The IL-10R2 binding site, defined by alanine-scanning mutagenesis, consists of Tyr51, Asn54, Arg55 on helix *A* and Tyr114 and Glu117 from helix *D* (Logsdon *et al.*, 2004). Interestingly, the IL-

22R1 and IL-10R2 binding sites map to the regions of IL-22 that exhibit the greatest structural differences between the NCS-related monomers (Fig. 6). The largest main-chain differences are located in the first 72 amino acids of IL-22_{Dm} and encompass the pre-*A*, helix *A* and the *AB* loop, regions that contact both IL-22R1 and IL-10R2 (Fig. 6). Smaller but significant changes are also observed for Tyr114 and Glu117 located on helix *D*, which suggests the entire IL-10R2 binding site can undergo correlated structural changes.

Since the structurally variable regions of IL-22 are located within the IL-22R1 and IL-10R2 binding sites, receptor-induced conformational changes may be important in assembling the IL-22 receptor complex. The structural differences between IL-22 monomers are consistent with recent data showing proteins exist as a population of conformational states, sometimes called a dynamic ensemble (Gunasekaran *et al.*, 2004). Based on our analysis of IL-22_{Dm}, the most structurally divergent areas of the ensemble correspond to the *AB* loop and the IL-10R2 binding site. This suggests IL-22R1 binding to IL-22 could shift the distribution of IL-22 conformational states towards an ensemble optimized for IL-10R2 binding. This model may explain in part why IL-10R2 binds to the IL-22/IL-22R1 complex more tightly than to IL-22 alone. A structural/energetic link between the IL-22R1 and IL-10R2 binding sites is also supported by studies conducted with monoclonal antibodies against the IL-10R2 binding site on IL-22 that increase the affinity of IL-22 for IL-22R1 (Li *et al.*, 2004). In addition, a similar mechanism of allosteric coupling between receptor-binding sites has recently been proposed for the growth-hormone receptor complex (Walsh *et al.*, 2004). While this 'conformational change' model is attractive, IL-22R1/IL-10R2 receptor contacts may also be important in increasing the affinity of IL-10R2 for the IL-22/IL-22R1 complex. Examples of receptor–receptor interactions have been observed in the ternary complexes of growth hormone and IL-6 (de Vos *et al.*, 1992; Boulanger *et al.*, 2003).

Although it has not been tested experimentally, Pro50 may also play an important role in IL-10R2 binding. Pro50 is conserved in all known IL-22 sequences and precedes Tyr51, Asn54 and Arg55, which form most of the IL-10R2 binding site (Fig. 7). Furthermore, in the IL-22/IL-22R1 homology model, Pro50 is located on the edge of the IL-22R1 binding interface, where it could contact IL-22R1 as well as IL-10R2 (Fig. 7). Thus, IL-22R1 binding to IL-22 could properly position Pro50 for interactions with IL-10R2. Interestingly, the Fc/FcγRIII complex structure provides an example where a proline and N-linked glycans are both directly involved in a binding interface (Sondermann *et al.*, 2000). In the Fc/FcγRIII complex, Pro329 from the Fc is sandwiched between Trp87 and Trp110 contributed from FcγRIII. Similar hydrophobic and aromatic residues are found in the sequence of IL-10R2 that could form a similar contact in the IL-22/IL-10R2 interface. In addition, the GlcNAc moiety attached to Asn297 of the Fc makes a hydrogen bond with Arg152 on FcγRIII, supporting the possibility that IL-10R2 forms direct interactions with glycans attached to Asn54.

3.7. Glycosylation in receptor binding

As described previously, N-linked carbohydrates attached to IL-22 have been shown to impact both IL-22R1 and IL-10R2 interactions (Logsdon *et al.*, 2004). To provide a structural model that explains this observation, IL-22_{Dm} monomer *D*, which has the most complete carbohydrate chain attached to Asn54, was superimposed onto the IL-22/IL-22R1 homology model. The position of the carbohydrate chain, as observed in the IL-22_{Dm} structure, partially shields IL-10R2 binding residues Tyr51 and Arg55. Based on the IL-22/IL-22R1 model, the position of the glycan at Asn54 in IL-22_{Dm} is not consistent with the receptor-binding data. However, the incorrect position of Asn54 caused by crystal contacts in the IL-22_{Dm} structure suggests that the proper orientation of Asn54 for IL-10R2 binding might be induced by IL-22R1 binding.

The importance of the position and chemistry of the $N^{\delta1}$ atom of Asn54 is emphasized by mutations of Asn54 to glutamine or aspartate, which essentially abolish IL-10R2 binding (Logsdon *et al.*, 2004). To define a more probable location for Asn54 and the associated carbohydrate, the position of the carbohydrate chain on Asn54 was evaluated, in the context of the IL-22_{Dm}/IL-22R1 model, at each of the nine possible side-chain rotamers for asparagines described by Lovell *et al.* (2000). One rotamer ($\chi_1 = -174^\circ$, $\chi_2 = 20^\circ$) exposed the IL-10R2 binding site to the solvent and positioned the carbohydrate chain in close proximity to the IL-22R1 chain between the two receptor domains (Fig. 7). In this position, the carbohydrate can make transient associations with IL-22R1, which is consistent with the twofold slower off-rate of IL-22 variants with carbohydrate at Asn54 *versus* those with only an asparagine (Logsdon *et al.*, 2004). Interestingly, the position of the *N*-acetyl group of the first GlcNAc is positioned towards the IL-22/IL-22R1 interface in a manner analogous to its contact in the IL-22 dimer interface (Fig. 4). In this position, the *N*-acetyl group may act as a lever to properly position Asn54 and the attached carbohydrate for interactions with IL-10R2. Structural studies on IL-22 receptor complexes to validate the mechanisms discussed are now under way.

This work was supported by the NIH (grant AI47300). Use of the Advanced Photon Source was supported by the US Department of Energy, Office of Science, Office of Basic Energy Sciences under contract No. W-31-109-Eng-38.

References

Adams, P. D., Pannu, N. S., Read, R. J. & Brünger, A. T. (1997). *Proc. Natl Acad. Sci. USA*, **94**, 5018–5023.
Aggarwal, S., Xie, M. H., Maruoka, M., Foster, J. & Gurney, A. L. (2001). *J. Interferon Cytokine Res.* **21**, 1047–1053.
Bazan, J. F. (1990*a*). *Cell*, **61**, 753–754.
Bazan, J. F. (1990*b*). *Proc. Natl Acad. Sci. USA*, **87**, 6934–6938.
Boulanger, M. J., Chow, D. C., Brevnova, E. E. & Garcia, K. C. (2003). *Science*, **300**, 2101–2104.
Brünger, A. T. (1992). *Nature (London)*, **355**, 472–474.

Brünger, A. T., Adams, P. D., Clore, G. M., DeLano, W. L., Gros, P., Grosse-Kunstleve, R. W., Jiang, J.-S., Kuszewski, J., Nilges, M., Pannu, N. S., Read, R. J., Rice, L. M., Simonson, T. & Warren, G. L. (1998). *Acta Cryst.* D**54**, 905–921.
Carson, M. (1997). *Methods Enzymol.* **277**, 493–505.
Chang, C., Magracheva, E., Kozlov, S., Fong, S., Tobin, G., Kotenko, S., Wlodawer, A. & Zdanov, A. (2003). *J. Biol. Chem.* **278**, 3308–3313.
Collaborative Computational Project 4, Number 4 (1994). *Acta Cryst.* D**50**, 760–763.
Dumoutier, L., Louahed, J. & Renauld, J. C. (2000). *J. Immunol.* **164**, 1814–1819.
Dumoutier, L., Van Roost, E., Colau, D. & Renauld, J. C. (2000). *Proc. Natl Acad. Sci. USA*, **97**, 10144–10149.
Fickenscher, H., Hor, S., Kupers, H., Knappe, A., Wittmann, S. & Sticht, H. (2002). *Trends Immunol.* **23**, 89–96.
Gunasekaran, K., Ma, B. & Nussinov, R. (2004). *Proteins*, **57**, 433–443.
Jiang, J. S. & Brünger, A. T. (1994). *J. Mol. Biol.* **243**, 100–115.
Josephson, K., Logsdon, N. J. & Walter, M. R. (2001). *Immunity*, **15**, 35–46.
Kabsch, W. (1976). *Acta Cryst.* A**32**, 922–923.
Kabsch, W. & Sander, C. (1983). *Biopolymers*, **22**, 2577–2637.
Kleywegt, G. J. & Jones, T. A. (1996). *Acta Cryst.* D**52**, 826–828.
Kotenko, S. V., Izotova, L. S., Mirochnitchenko, O. V., Esterova, E., Dickensheets, H., Donnelly, R. P. & Pestka, S. (2001). *J. Biol. Chem.* **276**, 2725–2732.
Krause, C. D., Mei, E., Xie, J., Jia, Y., Bopp, M. A., Hochstrasser, R. M. & Pestka, S. (2002). *Mol. Cell Proteomics*, **1**, 805–815.
Laskowski, R. J., MacArthur, M. W., Moss, D. S. & Thornton, J. M. (1993). *J. Appl. Cryst.* **26**, 283–290.
Lejeune, D., Dumoutier, L., Constantinescu, S., Kruijer, W., Schuringa, J. J. & Renauld, J. C. (2002). *J. Biol. Chem.* **277**, 33686–33682.
Li, J. *et al.* (2004). *Int. Immunopharmacol.* **4**, 693–708.
Logsdon, N. J., Jones, B. C., Allman, J. C., Izotova, L., Schwartz, B., Pestka, S. & Walter, M. R. (2004). *J. Mol. Biol.* **342**, 503–514.
Logsdon, N. J., Jones, B. C., Josephson, K., Cook, J. & Walter, M. R. (2002). *J. Interferon Cytokine Res.* **22**, 1099–1112.
Lovell, S. C., Word, J. M., Richardson, J. S. & Richardson, D. C. (2000). *Proteins*, **40**, 389–408.
Nagem, R. A., Colau, D., Dumoutier, L., Renauld, J. C., Ogata, C. & Polikarpov, I. (2002). *Structure*, **10**, 1051–1062.
Otwinowski, Z. & Minor, W. (1997). *Methods Enzymol.* **276**, 307–326.
Pestka, S., Krause, C. D., Sarkar, D., Walter, M. R., Shi, Y. & Fisher, P. B. (2004). *Annu. Rev. Immunol.* **22**, 929–979.
Read, R. J. (2001). *Acta Cryst.* D**57**, 1373–1382.
Sondermann, P., Huber, R., Oosthuizen, V. & Jacob, U. (2000). *Nature (London)*, **406**, 267–273.
Vos, A. M. de, Ultsch, M. & Kossiakoff, A. A. (1992). *Science*, **255**, 306–312.
Walsh, S. T., Sylvester, J. E. & Kossiakoff, A. A. (2004). *Proc. Natl Acad. Sci. USA*, **101**, 17078–17083.
Walter, M. R. (2002). *Immunol. Res.* **26**, 303–308.
Walter, M. R. (2004). *Adv. Protein Chem.* **68**, 171–223.
Walter, M. R. & Nagabhushan, T. L. (1995). *Biochemistry*, **34**, 12118–12125.
Winn, M. D., Ashton, A. W., Briggs, P. J., Ballard, C. C. & Patel, P. (2002). *Acta Cryst.* D**58**, 1929–1936.
Wolk, K., Kunz, S., Witte, E., Friedrich, M., Asadullah, K. & Sabat, R. (2004). *Immunity*, **21**, 241–254.
Xie, M. H., Aggarwal, S., Ho, W. H., Foster, J., Zhang, Z., Stinson, J., Wood, W. I., Goddard, A. D. & Gurney, A. L. (2000). *J. Biol. Chem.* **275**, 31335–31339.
Xu, T., Logsdon, N. J. & Walter, M. R. (2004). *Acta Cryst.* D**60**, 1295–1298.